Int J Fract (2025) 249:76
https://doi.org/10.1007/s10704-025-00892-w

RESEARCH

Crystal plasticity-based intergranular facture simulation of AA 5083 aluminum alloy for tri-junction grain boundary

Xin Zhang · Qi Zhao · Hongxia Zhang · Zhipeng Zhai · Xiang Chen · Ying Hu · Zhuo Han · Nianfeng Zhang · Yucheng Gui · Magd Abdel Wahab

Received: 30 May 2025 / Revised: 1 October 2025 / Accepted: 5 October 2025

Abstract The fracture mode of AA 5083 Al–Mg alloy is predominantly intergranular. For this, a three-dimensional Crystal Plasticity Finite Element (CPFE) model is developed to investigate Grain Boundary (GB) fracture behavior under uniaxial tensile loading. Following parameter calibration, the simulated tensile strength demonstrates consistency with experimental data, with a high accuracy of 97%. Furthermore, by integrating CPFE model incorporating the dislocation slips with a GB model, a two-dimensional tri-junction crystal plasticity framework is established, and cohesive elements are implemented within the three grains to simulate GB fracture process under uniaxial tension. This tri-junction model shows a good convergence. The effect of grain orientation, location and GB thickness on GB fracture is investigated. The results reveal that grain orientation and location significantly influences GB fracture behavior. It is found that the Goss-Brass-P orientation combination demonstrates the optimal comprehensive mechanical properties, achieving a strain energy density of 7.09 MJ/m^3. Furthermore, there exists a threshold effect about GB thickness on comprehensive property. The optimal performance is obtained when the cohesive that determines GB thickness is set to 2.

Keywords Grain boundary fracture · AA 5083 Al–Mg alloy · Crystal plasticity · Tri-junction crystal plasticity model

X. Zhang · Q. Zhao (✉) · H. Zhang (✉) · Z. Zhai · X. Chen · Y. Hu · Z. Han · N. Zhang · Y. Gui
School of Automotive Materials, Hubei University of Automotive Technology, Shiyan 442002, China
e-mail: zhaoqihuat@163.com

H. Zhang
e-mail: zhx@huat.edu.cn

M. Abdel Wahab
Soete Laboratory, Faculty of Engineering and Architecture, Ghent University, Technologiepark Zwijnaarde 903, B-9052 Zwijnaarde, Belgium

M. Abdel Wahab
Parallel and Distributed Systems Laboratory, Jožef Stefan Institute, Jamova Cesta 39, SI-1000 Ljubljana, Slovenia

M. Abdel Wahab
College of Engineering, Yuan Ze University, Taiwan, China

1 Introduction

Global climate mitigation efforts have positioned lightweighting as a critical strategy, with cast aluminum alloys emerging as the prime material for carbon reduction due to their superior properties (Miller et al. 2017). Recent smelting advancements have substantially lowered aluminum costs, while expanded specifications and enhanced performance enable broader adoption, particularly in transportation systems (Du et al. 2011; Geng et al. 2023).

Published online: 17 October 2025

AA5083 Al–Mg alloy, known for its excellent corrosion resistance, weldability, formability, and high specific strength, is widely used in various fields (Kramer et al. 2012). However, as a non-heat-treatable Al–Mg alloy with a relatively high magnesium content, the β phase (Al_3Mg_2) may precipitate along GBs or within grains (Bessone et al. 1992), increasing the alloy's susceptibility to Stress Corrosion Cracking (SCC) and intergranular corrosion. Prior studies have demonstrated that GBs enhance material strength by restricting dislocation motion, while also influencing ductility and fatigue performance (Randle and Ralph 1988). Subsequent research employing simulations has revealed that Co and Ti segregation at GBs significantly alters the mechanical behavior of aluminum bicrystals, primarily through suppressing plastic deformation mechanisms, modifying deformation pathways, reducing crack propagation rates, and improving fatigue life (Babicheva et al. 2017). However, the formation of microcracks at GB is still inevitable. Subsequently, researchers have focused on the study of microcracks, aiming to further understand and mitigate their impact on the alloy's performance (Pouillier et al. 2012).

Despite significant advancements in mitigating hot cracking through previous research (Nasibullina et al. 2019; Zhao et al. 2018), the complete elimination of crack formation remains elusive. While experimental techniques have enabled the observation of microcracks, capturing the full sequence of microcrack initiation, propagation, and ultimate failure continues to present substantial challenges (Hajshirmohammadi and Khonsari 2020). This limitation has motivated extensive utilization of numerical simulation approaches to address these complex phenomena.

The Crystal Plasticity Finite Element Method (CPFEM) (Roters et al. 2010) has emerged as a powerful tool for characterizing the mechanical response and associated deformation behavior of metallic materials, effectively bridging the gap between macroscopic boundary conditions and microstructure interactions. The theoretical foundations of CP were established through the kinematic and geometric formulations developed by Hill and Rice (1972), with subsequent advancements by Asaro and Needleman (1985), who implemented these principles in finite element analyses of copper's mechanical behavior. Further developments include Zhao et al.'s (2019) model correlating Flexible Printed Circuit resistance with microstructural parameters such as grain orientation, grain quantity, grain size, and slip band distribution.

Recent CPFEM advances enable precise material modeling. Huang et al. developed a shear strain-based model predicting magnesium alloy damage through slip system analysis (Huang et al. 2018). Künkler et al.'s (2008) 2D framework captured short crack propagation and slip plane transitions, highlighting grain orientation/size effects (2008). Figueiredo and Chou established GB correlations with HP/IHP behaviors (Figueiredo et al. 2023; Chou and Pande 1972), integrating their models into CPFEM software for enhancing the simulations (Han and Yi 2021).

While extensive experimental research has been conducted on GB fracture in cast alloys (Cantwell et al. 2014; Winning et al. 2001; Gorkaya et al. 2011), the simulation of this phenomenon using CPFE methods remains limited. While the microscopic mechanisms of GB fracture such as dislocation-GB interactions, atomic-scale reconfigurations, and crack nucleation have been extensively studied, existing simulations struggle to capture macroscale mechanical responses. Traditional models often oversimplify GB behavior through phenomenological constitutive relations, neglecting the critical role of crystallographic orientations in real fracture processes. Such oversights lead to unreliable predictions of GB crack propagation paths.

The tensile fracture characteristics of AA5083 cast aluminum alloy, where damage typically initiates at GBs and propagates along, underscore the critical role of GBs in determining the alloy's mechanical properties. This fundamental understanding has guided our selection of AA5083 cast aluminum alloy as the primary material for this investigation.

Based on the foundational work of previous scholars (Zhao et al. 2021; Qu et al. 2024), this study implements a comprehensive computational framework that integrates CPFE model incorporating dislocation slip mechanisms with GB fracture model. A two-dimensional model with explicitly defined grain orientations is developed. The maximum nominal stress damage criterion is implemented through a User-Defined Material Subroutine (UMAT) to simulate damage initiation and subsequent crack propagation along GBs. This integrated method successfully captured the micromechanical GB fracture behavior and tensile properties of the material system. The

developed model provides an effective tool for investigating GB fracture mechanisms during uniaxial tensile deformation of AA5083 cast alloy, offering new insights into the interplay between crystallographic orientation, dislocation activity, and intergranular fracture.

The article structure is organized as follows. Section 2 outlines materials, experimental methods, CPFEM theory, and GB fracture principles. Section 3 presents the CPFE model. Section 4 systematically analyzes critical mechanisms: Sect. 4.1 calibrates material parameters using tensile data; Sect. 4.2 assesses mesh size effects and model convergence; Sect. 4.3 discusses tensile stress contours; Sect. 4.4 Experimental modelling observation; Sect. 4.5 quantifies strain rate sensitivity (n) under low-strain conditions; Sect. 4.6 studies the influence of tensile strain on GB fracture; Sect. 4.7 investigates the effect of spatial arrangement in identical grain combinations; Sect. 4.8 examines crystal orientation effects on GB stress–strain distribution and Sect. 4.9 predicts GB thickness-dependent fracture behavior. Finally, Sect. 5 presents the conclusions.

2 Materials and numerical method

2.1 Material and experimental

AA5083 aluminum alloy specimens (chemical composition: Si 0.40%, Fe 0.40%, Cu 0.10%, Mn 0.70%, Mg 4.50%, Zn 0.25%, Ti 0.15%, Cr 0.25%, bal. Al) were prepared through recrystallization at 460 °C for 1 h followed by water quenching, with subsequent aging at 150 °C for 7 days to obtain equiaxed grains. Building upon the experimental investigation of GB fracture in this material by Pouillier et al. (2012), we compared the simulated stress–strain curves with the experimental measurements, and the size of tensile test specimen is shown in FIg. 1. Furthermore, leveraging the EBSD maps provided in their work, we established a model for simulating GB fracture mechanisms.

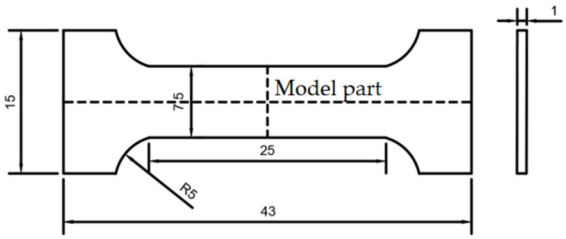

Fig. 1 Stretching specimen schematic diagram

2.2 Crystal plasticity theory

Based on the seminal work of McHugh et al. (1993) and Pierce et al. (1983), the deformation gradient tensor (F) and velocity gradient tensor (L) are expressed by:

$$\begin{cases} F = F_{\mathrm{e}} \cdot F_p \\ L = L_e + F_e \cdot L_p \cdot F_e^{-1} \end{cases} \tag{1}$$

where $F_{\mathrm{e}} \cdot F_p$, L_e and L_p are the elastic, plastic, elastic, and plastic velocity gradients, respectively.

The plastic deformation gradient evolution rate and the slip shear rate on the α slip system maintain the following relationship:

$$L^p = \sum\nolimits_{\alpha=1}^{N} \dot{\gamma} s_\alpha^* \otimes m_\alpha^* \tag{2}$$

where s_α^* is the slip direction vector of the α slip system, and m_α^* is the normal direction vector to the slip plane that is perpendicular to all vectors on the slip plane.

The Jaumann rate $\underset{\sigma}{\nabla} *$ is related to the lattice's symmetric stretch rate D^* as follows:

$$\underset{\sigma}{\nabla} * + \sigma(I : D) = C : D \tag{3}$$

where I represents the second-order identity tensor, and C represents the fourth-order elasticity tensor.

The partial shear stress $\gamma^{(\alpha)}$ on the slip system is related to the current stress:

$$\gamma^{(\alpha)} = m^{*(\alpha)} \cdot (\rho_0/\rho) \cdot s^{*(\alpha)} \tag{4}$$

where ρ_0 and ρ are the mass densities of the reference state and the current state, respectively.

Based on Schmid's law, the power-law model proposed by Hutchinson (1976) is used to describe the relationship between the hardening equation and the rate. The shear rate $\dot{\gamma}^{(\alpha)}$ of the α slip system is related to the Schmid stress and satisfies:

$$\dot{\gamma}^{(\alpha)} = \dot{\gamma}_0^{(\alpha)} \mathrm{sgn}(\gamma^{(\alpha)}/g^{(\alpha)}) |\gamma^{(\alpha)}/g^{(\alpha)}|^n \tag{5}$$

where $\dot{\gamma}^{(\alpha)}$ is the reference strain rate for the α slip system, $g^{(\alpha)}$ represents the strength of the slip system and n is the rate sensitivity index.

The hardening strength can be expressed as:

$$\dot{g} = \sum_{\beta=1}^{N} h_{\alpha\beta}\dot{\gamma}^{\beta} \tag{6}$$

where $h_{\alpha\beta}$ is the slip hardening modulus. When $\alpha = \beta$, it is called the self-hardening modulus and when $\alpha \neq \beta$, it is called the latent-hardening modulus. The self-hardening modulus can be described as (Peirce et al. 1982):

$$h_{\alpha\alpha} = h_0 \mathrm{sech}^2 |h_0\gamma/(\gamma_s - \gamma_0)| \tag{7}$$

where h_0 is the initial hardening modulus and γ_0 is the current strength's initial value. γ_s is the breakthrough stress at which large plastic flow occurs, and γ is the Taylor accumulated shear strain on all slip systems. The latent-hardening modulus can be described as:

$$h_{\alpha\beta} = h_{\alpha\alpha}[q + (1-q)\delta^{\alpha\beta}] \tag{8}$$

where $\delta^{\alpha\beta}$ is the Kronecker delta.

2.3 GB fracture theory

Following the work of Rohith et al. (2019), a cohesive zone GB fracture model is established to characterize interfacial damage progression, as shown in Fig. 2. (a) Schematic diagram of cohesive elements insertion (Fig. 2). (a) Schematic diagram of cohesive elements insertiona illustrates the geometric configuration of cohesive zone elements embedded into a finite element model. These cohesive elements are inserted into FE mesh to simulate failure behaviors at material interfaces or within materials, such as crack propagation or delamination (Fig. 2). (a) Schematic diagram of cohesive elements insertionb shows the cohesive force–displacement relationship curve for the cohesive elements, describing the mechanical behavior of the interface. The curve consists of two phases, namely an initial elastic phase and a softening phase. In the initial elastic phase, the slope of the curve is E, representing the initial stiffness of the interface. When the displacement reaches a critical value l_0, damage initiation occurs at the interface, corresponding to a critical stress σ_c. In the condition of plane strain, the initial cohesive strength is approximately 3 times of material yield stress (Liu et al. 2009). The yield stress of this studied AA5083 alloy is 110 MPa, and thus σ_c is equal to 330 MPa. As displacement increases further, the interface enters the softening phase, where the stress gradually decreases until complete failure (damage ending). The area under the curve represents the fracture energy G_{IC}, which characterizes the fracture toughness of the interface.

Following Mao Xiao's theoretical framework (Xiao et al. 2024), let n, s, and t represent the normal and two tangential directions of the cohesive elements, respectively. The strain-separation relationship can then be expressed as:

$$\begin{Bmatrix} \delta_n \\ \delta_s \\ \delta_t \end{Bmatrix} = T \begin{Bmatrix} \varepsilon_n \\ \varepsilon_s \\ \varepsilon_t \end{Bmatrix} \tag{9}$$

The thickness referenced here corresponds to the intrinsic thickness of the cohesive element, which is

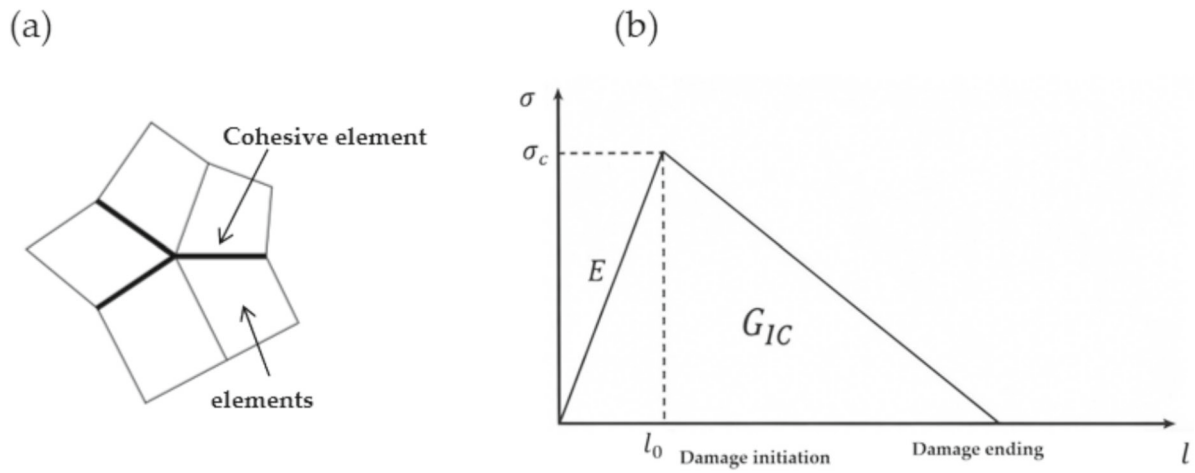

Fig. 2 **a** Schematic diagram of cohesive elements insertion and **b** cohesive fracture model schema

conventionally assigned a unit value (1) in cohesive zone modeling for numerical normalization. The physical thickness of the cohesive element is negligible, asymptotically approaching zero. The constitutive behavior of the cohesive element follows a linear elastic relationship between strain and stress:

$$\begin{Bmatrix} \sigma_n \\ \sigma_s \\ \sigma_t \end{Bmatrix} = \begin{pmatrix} C_1 & 0 & 0 \\ 0 & C_2 & 0 \\ 0 & 0 & C_3 \end{pmatrix} \begin{Bmatrix} \varepsilon_n \\ \varepsilon_s \\ \varepsilon_t \end{Bmatrix} \tag{10}$$

where σ_n denotes the normal stress component, while σ_s and σ_t represent the two orthogonal shear stress components,. The corresponding stiffness parameters (C_1, C_2, C_3) exhibit the following thickness-dependent constitutive relationship:

$$C_1 = \frac{E}{T}, C_2 = \frac{G}{T}, C_3 = \frac{G}{T} \tag{11}$$

When displacement is applied to a triple-junction grain model, complex stresses arise at GBs. Equation (11) shows the normal stress σ_n couples with orthogonal shear stresses σ_s and σ_t, affecting boundary stability. Thickness-dependent stiffness parameters cause varied mechanical responses across different boundary positions.

The cohesive element damage modeling in Abaqus offers two fundamental initiation criteria, namely the maximum nominal stress criterion (for tensile failure) and the minimum nominal stress criterion (for compressive failure).

In triple-junction modeling, monitoring boundary stresses with these criteria predict damage initiation. Stress meeting criteria triggers damage evolution, compromising material performance:

$$\begin{aligned} &\max\left\{\frac{\sigma_n}{\sigma_0}, \frac{\sigma_s}{\sigma_0}, \frac{\sigma_t}{\sigma_0}\right\} = 1 \\ &\left(\frac{\sigma_n}{\sigma_0}\right)^2 + \left(\frac{\sigma_s}{\sigma_0}\right)^2 + \left(\frac{\sigma_t}{\sigma_0}\right)^2 = 1 \\ &\max\left\{\frac{\varepsilon_n}{\varepsilon_0}, \frac{\varepsilon_s}{\varepsilon_0}, \frac{\varepsilon_t}{\varepsilon_0}\right\} = 1 \end{aligned} \tag{12}$$

$$\left(\frac{\varepsilon_n}{\varepsilon_0}\right)^2 + \left(\frac{\varepsilon_s}{\varepsilon_0}\right)^2 + \left(\frac{\varepsilon_t}{\varepsilon_0}\right)^2 = 1 \tag{13}$$

3 CPFEM

3.1 Tensile model

Based on symmetry principles, a one-eighth symmetric sub-model of the specimen is adopted for simulation to reduce computational costs while maintaining mechanical representativeness.

As shown in Fig. 3, a polycrystalline geometric tensile model is established, and the size of this model is 21.5 × 7.5 × 0.5 mm. A polycrystalline finite element model composed of 200,000 randomly oriented grains is generated, with each grain consisting of approximately 2 hexahedral elements (C3D8). The model size was uniformly scaled down based on the tensile specimen dimensions.

A multi-scale meshing strategy was implemented, featuring progressively coarser element sizing from GB regions to the grain interiors, thereby achieving significant computational savings while maintaining solution accuracy in critical areas. The left end of the model is fixed on the YOZ plane, with constraints applied in the U1, U2, U3, UR1, UR2, and UR3 directions (i.e., U1 = 0, U2 = 0, U3 = 0, UR1 = 0, UR2 = 0, UR3 = 0). A reference point is established at the middle position on the outer side of the right end of the model, coupled with the YOZ plane at the right end. Tensile simulations are performed by applying displacement boundary conditions through this reference point, with a tensile displacement set to 1.075 mm.

Once the parameters of the tensile model are determined, a polycrystalline finite element model composed of three grains with different orientations is established, as shown in Fig. 4. The model size is 1.5 mm × 1 mm. The left end of the model is fixed, with constraints applied in the U1, U2, and U3 directions (i.e., U1 = 0, U2 = 0, U3 = 0). A reference point is established at the middle position on the outer side of the right end of the model, coupled with the right end. Tensile simulations are conducted by applying boundary displacements driven by the reference point, with a tensile displacement set to 0.12 mm. The monocrystalline domains are discretized using four-node bilinear plane strain quadrilateral elements (CPE4), while A 4-node two-dimensional cohesive element(COH2D4) are implemented to simulate the tri-crystalline GB interfaces. In Fig. 4, the leftmost grain is designated as Grain 1, the grain at the upper-

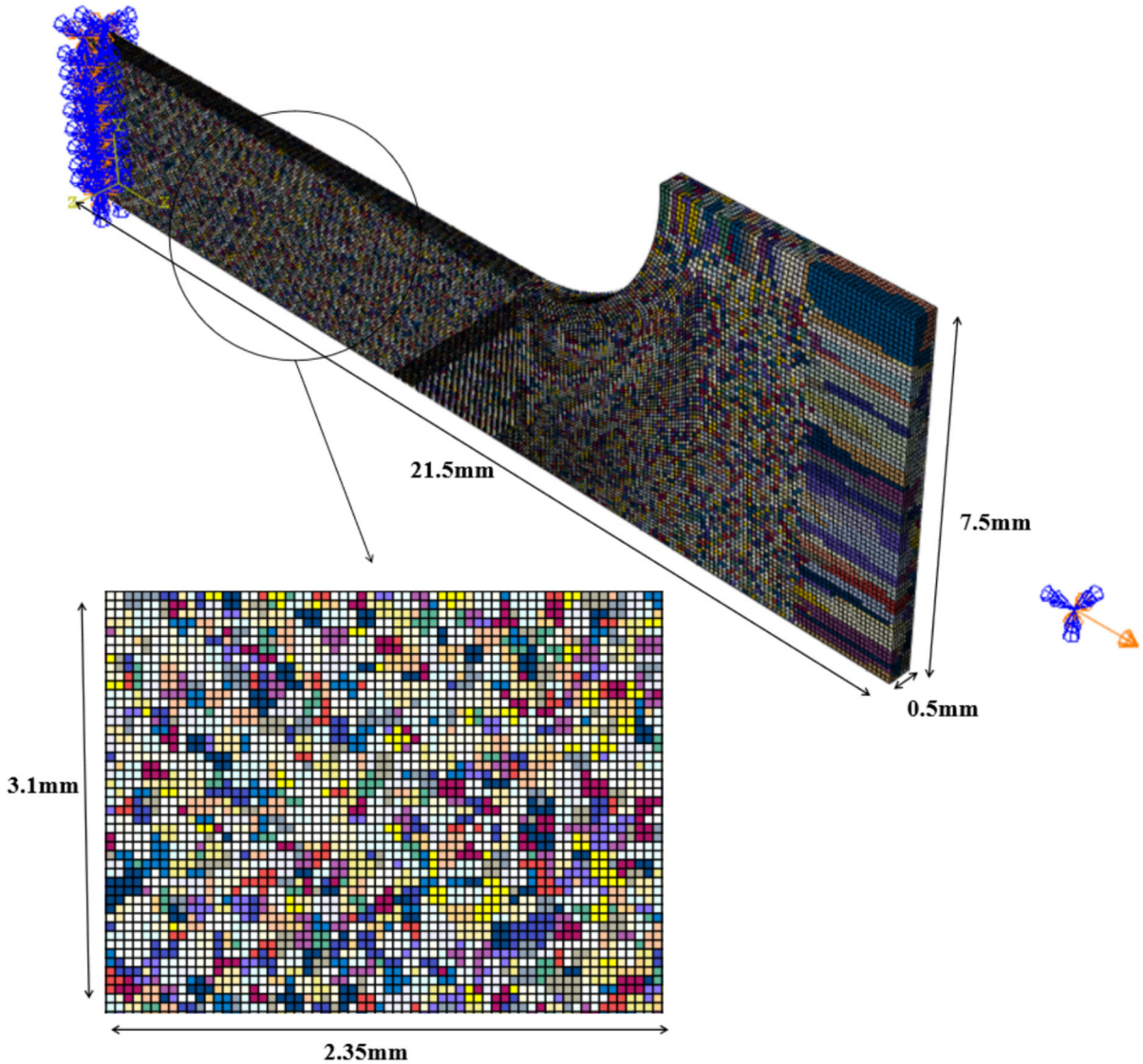

Fig. 3 CPFE model for tensile deformation

right corner as Grain 2, and the grain at the lower-left corner as Grain 3. The central triple junction region, where these three grains converge, constitutes the GBs.

4 Results and discussions

4.1 Parameter calibration

Using the uniaxial tensile model established in this paper, the constants of the CP model (C_{11}, C_{12}, and C_{44}), initial hardening modulus, saturation stress, and initial critical shear stress are adjusted to calibrate the tensile stress–strain curves, and the simulation results are compared with the experimental results. Calibrated crystal plasticity parameters for AA 5083 material are shown in Table 1. And the implemented cohesive element parameters are presented in Table 2. Figure 5 presents a comparison between the experimental results and the simulated stress–strain curves using the crystal plasticity parameters, indicating a good match between the simulation and experimental outcomes, with an accuracy of 97%. This confirms

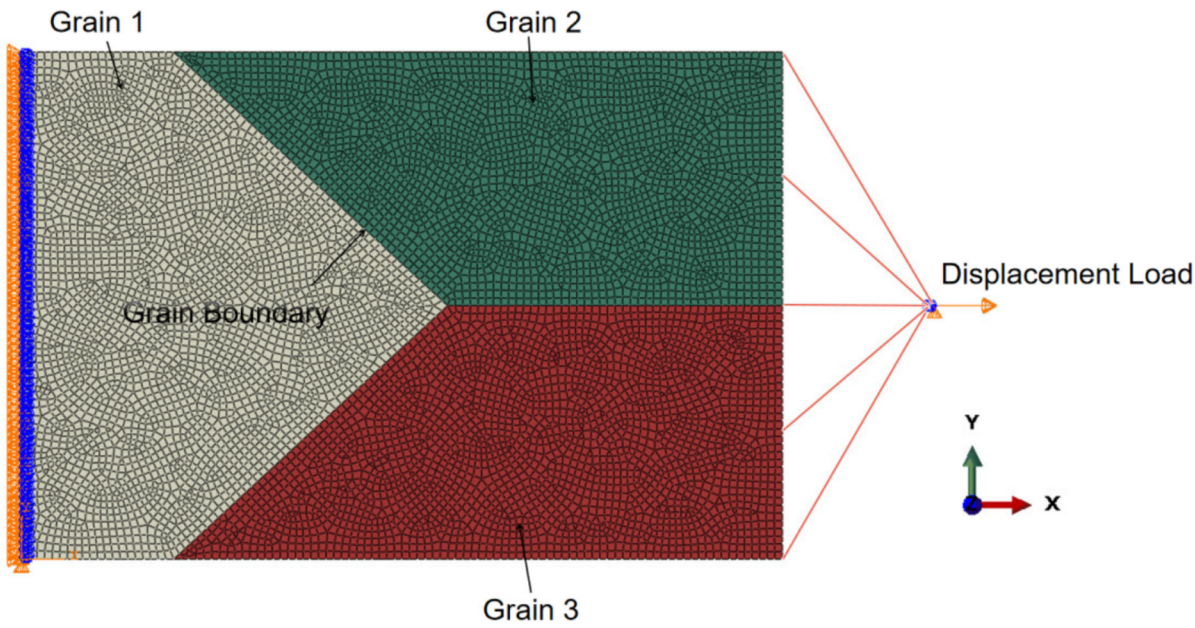

Fig. 4 Tri-junction model for tensile deformation

Table 1 Implanted CP constitutive parameters of AA 5083 alloy

n	γ	h_0/ MPa	τ_s/ MPa	τ_0/ MPa	q	C_{11}/ MPa	C_{12}/ MPa	C_{44}/ MPa
3	0.001	40	33	11.2	1	88,350	60,410	28,340

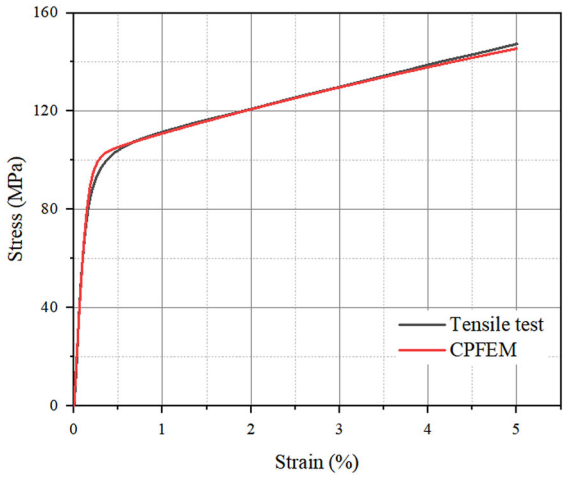

Fig. 5 Comparison of the stress–strain curves between simulation and experimental results

the accuracy of the CP model and parameters employed in this paper.

It is worthy to note that C11, C12, and C44 serve as fitting parameters for the crystalline elasticity model. C11 represents the longitudinal stiffness constant, reflecting the crystal's resistance to deformation along its cubic crystal axes during uniaxial tensile or compressive loading. During the fitting process, the value of C11 predominantly determines the slope of the elastic stage; this slope increases as C11 values rise. C12 represents the transverse stiffness constant. During fitting, increasing C12 causes the fitted curve to contract inward, reducing the slopes of both the elastic and plastic stages. C44 represents the shear stiffness constant. Increasing C44 during fitting leads to higher values on the stress–strain curve. These parameters cannot be directly obtained through the

Table 2 Material parameters of cohesive element

Parameters	G_{IC}(J/mm)	C_1/MPa	C_2/MPa	C_3/MPa	σ_n(MPa)	σ_s	σ_t
Value	35	167,200	63,768	63,768	80	80	80

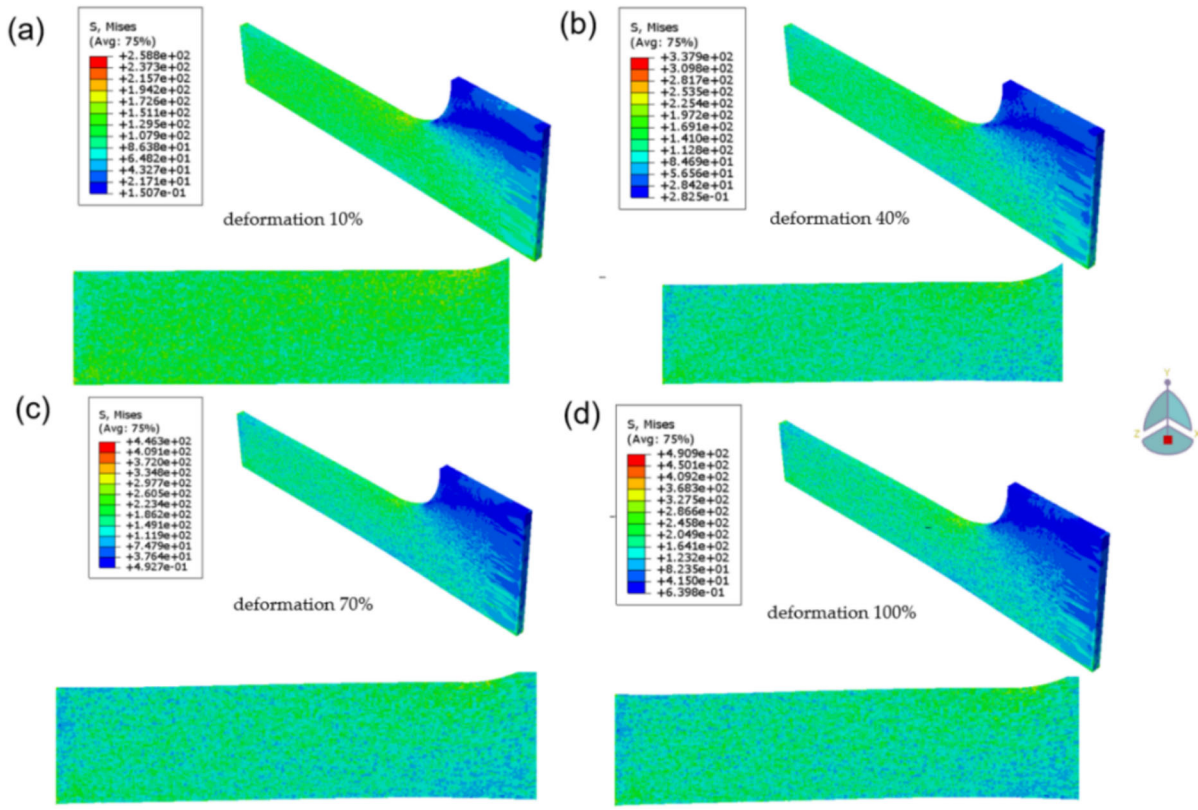

Fig. 6 Stress distribution of the CP model: **a** deformation 10%, **b** deformation 40%, **c** deformation 70%, **d** deformation 100%

experimental measurement, but can be determined from the stress–strain data through the above fitting method. By adjusting C11, C12, and C44 parameters, we obtain the best match between the model's stress–strain curve and experimental one.

4.2 The stress contour plots of tensile models

From a numerical perspective, the stress increases with strain accumulation, where the maximum stress rises from 258.8 to 490.9 MPa. During the initial stage, the stress distribution remains relatively uniform. However, as the strain magnitude increases, stress dilution occurs in localized regions, exhibiting distinct characteristics from the onset. The stress-diluted zones expand symmetrically with further strain progression. Regardless of the applied strain level, the transition regions consistently exhibit significantly higher stress concentrations compared to adjacent areas (Fig. 6).

This phenomenon arises because, during the initial yielding phase, plastic deformation is predominantly governed by primary slip systems exhibiting the lowest Critical Resolved Shear Stress (CRSS). The limited activation of slip systems (typically fewer than three independent slip systems) (Roters et al. 2010) restricts dislocation slip paths, resulting in the development of a quasi-uniform stress field across the

material volume. Subsequent strain accumulation activates additional slip systems, leading to increased dislocation density and intensified local stress concentrations.

The stress concentration in the transition region arises from geometric incompatibility effects that induce pronounced local stress gradients in areas subjected to bending deformation (Arsenlis and Parks 1999). This observation aligns fully with Hosford's theoretical framework on orientation-dependent slip system sensitivity during incipient plastic deformation (Hosford 2010).

4.3 Convergence of the tri-juction model

The calibrated parameters are implemented into the triple-junction GB model and analyze its convergence. Figure 7 demonstrates the influence of mesh refinement on the two-dimensional three-grain tensile model. To maintain the model's integrity and isolate the mesh size effect, all other parameters including the relative positions and dimensions of the three grains are kept constant throughout the analysis. One pole from the {111} polar plot is selected for analysis.

Mesh refinement critically influenced orientation representation as follows. At 30 μm, sparse pole distribution reflectes insufficient resolution for capturing localized deformation and orientation gradients. Reducing to 27.5 μm triggers pole clustering with elliptical symmetry, indicating enhanced microstructural sensitivity without spatial contraction. Further refinement to 25 μm intensifies clustering around preferred orientations, demonstrating improved texture evolution tracking. Continued reductions (20–15 μm) yields homogenized distributions with sharpened contours, achieving deformation uniformity while maintaining morphological stability evidence of diminishing returns beyond critical refinement thresholds. Notably, mesh refinement increases the maximum cumulative plastic strain in SDV121 from 36 to 50.8%, while reducing fracture-initiation strain from 18 to 12% demonstrates an enhanced computational accuracy with finer discretization.

These systematic variations validate model convergence. Progressive mesh reduction transformed dispersed poles into clustered configurations, establishing orientation homogeneity and numerical stability. The transition from macro-scale dispersion (< 30 μm) to microstructurally resolved clustering (> 25 μm) confirms the framework's capacity to balance detail capture with predictive robustness.

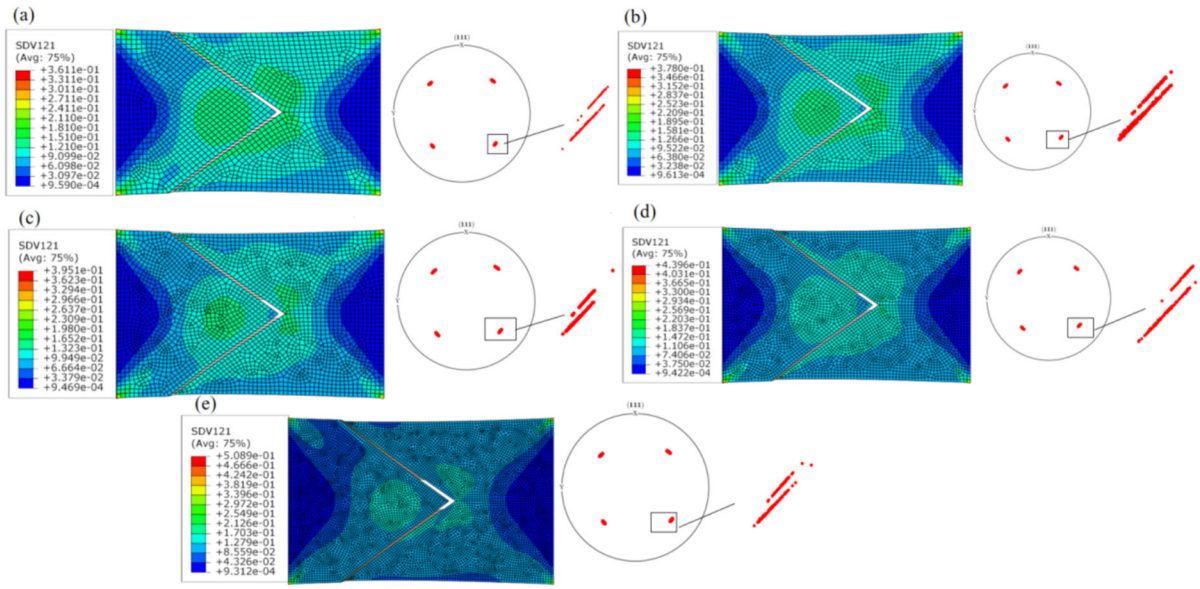

Fig. 7 The influence of grid size on GB fracture behavior: **a** mesh size 30 μm, **b** 27.5 μm, **c** 25 μm, **d** 20 μm, **e** 15 μm—SDV 121 represents the accumulative plastic strain

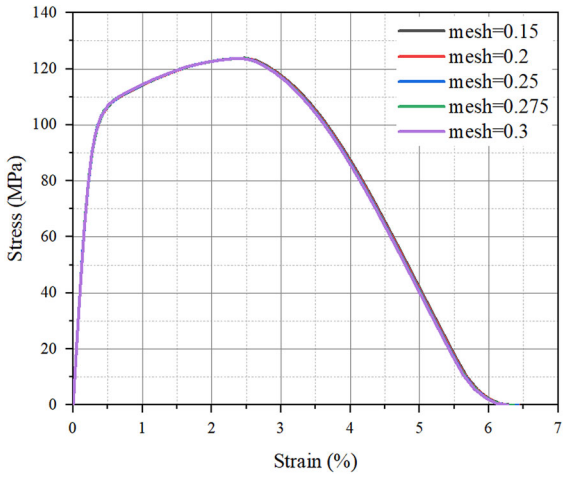

Fig. 8 Simulation results of GB fracture in tri-junction model

Consistent contour morphology during refinement further substantiates the model's reliability fulfills the key criteria for computational validation through controlled error minimization and solution reproducibility.

As it can be seen from Fig. 8, the stress–strain curves under different mesh divisions exhibit nearly identical trends. Prior to reaching the tensile strength, the curves almost coincide. After entering the necking stage, larger mesh sizes demonstrate greater deviations in the curves, though these deviations remain within 1%. This observation effectively validates the excellent convergence characteristics of the CP model.

4.4 Experimental modelling observation

To investigate the processes of grain deformation and GB fracture during practical tensile experiments. Based on the microstructural data derived from EBSD images in Pouillier et al. (2012), a two-dimensional model with dimensions of 1.5 mm × 1 mm was constructed in Fig. 9. This model is subjected to an applied strain of 0.05, enabling systematic observation of grain deformation characteristics and GB fracture behavior across varying strain levels.

Figure 10 illustrates a polycrystalline structure with randomly oriented grains, while Fig. 11 shows the Euler angles of the crystal grains in the EBSD map: upper left (45°, 90°, 180°), lower left (45°, 54.74°, 180°), upper right (45,° 63.43°, 90°), and lower right (45°, 35.26°, 45°). At low strain levels, the stress distribution within individual grains is relatively homogeneous, with elevated stresses primarily localized in bent regions. When the strain reaches approximately 40% of the total deformation, stress begins to concentrate in localized zones, marking the onset of heterogeneous stress distribution. The stress near GBs exceeds that in grain interiors by 20–30%. In the simulated cohesive elements representing GBs, the stress reaches a minimum, indicating imminent boundary fracture. With further strain accumulation, GB fracture initiates and propagates. Notably, fracture progression halts at bent regions. Comparative analysis of stress magnitudes reveals that bent regions exhibit maximum stresses of 315 MPa and 395 MPa in Figs. 10 and 11, respectively, whereas average stresses in other regions are 185 MPa and 230 MPa, representing a 50–70% increase.

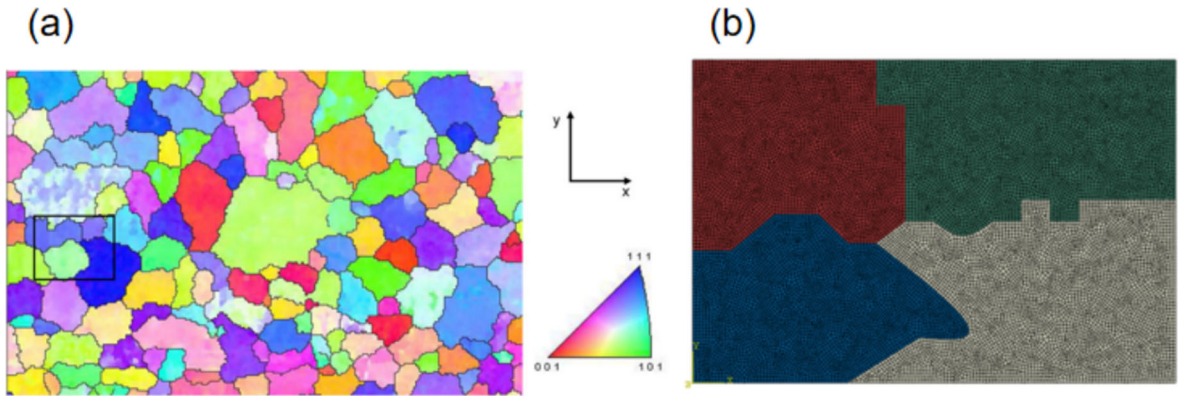

Fig. 9 **a** Grain color map of the zone studied by EBSD (Pouillier et al. 2012) and **b** CPFEM model

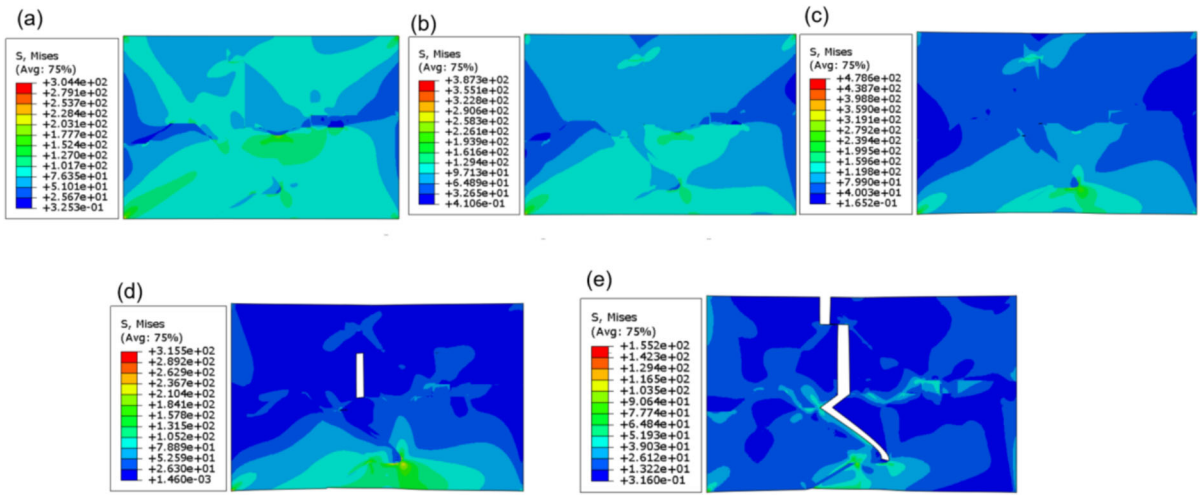

Fig. 10 Stress distribution in randomly oriented CP models for different percentages of deformation: **a** 5%, **b** 10%, **c** 40%, **d** 70% and **e** 100%

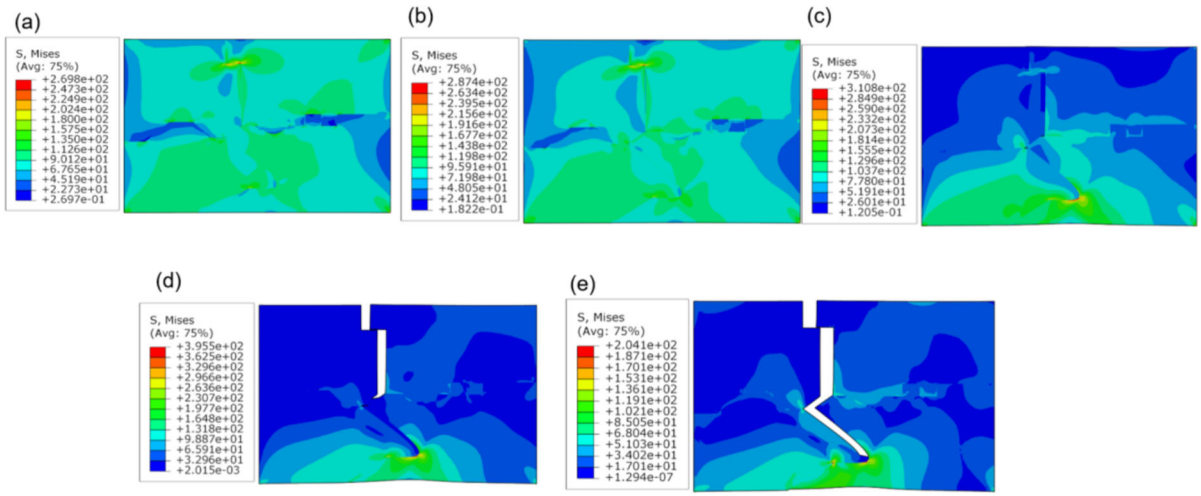

Fig. 11 Stress distribution in the CP models based on EBSD-measured orientations for different percentages of deformation: **a** 5%, **b** 10%, **c** 40%, **d** 70% and **e** 100%

A comparison of GB fracture initiation between Figs. 10 and 11 demonstrates distinct patterns. In Fig. 10, fracture initiates at the mid-section of GBs and propagates bidirectionally, whereas in Fig. 11, fracture initiates at the upper boundary and progresses downward. This suggests that grain orientation influences fracture initiation sites. The elevated stress near GBs arises from their constraining effect on dislocation motion, leading to localized stress accumulation (Rohoman and Zhou 2025). The significantly higher stresses observed at the bending boundaries are consistent with the findings reported by Arzt (Arzt 1998), which can be attributed to strain gradients generated during plastic bending. These strain gradients promote the accumulation of geometrically necessary dislocations (GNDs) near GBs. Such GNDs impede subsequent dislocation motion, thereby resulting in localized strengthening.

4.5 The influence of the strain rate sensitivity index (n) on the stress–strain curve

In CPFE models, the strain rate sensitivity coefficient n is a key parameter that directly affects the material's

hardening behavior and plastic deformation capacity. A higher n value typically indicates a stronger strain hardening capacity, which is closely related to the material's dislocation density, slip system activity, and GB effects. Previous studies have determined that the strain rate sensitivity coefficient (n) for most materials typically ranges from 10 to 50 (Kocks and Mecking 2003; Song et al. 2025). Moreover, adjusting n has a limited impact on the stress–strain curve. However, in the simulation process of this study, due to the selected material having relatively low levels of stress and strain, n has a significant influence on the simulation results under low stress–strain conditions. To systematically investigate this phenomenon, a series of simulations were conducted with varying n values while maintaining constant parameters (h_0 = 40 MPa, τ_s = 33 MPa,τ_0 = 11.2 MPa,γ = 0.001 s^{-1}).

The simulation results, presented in Fig. 12, reveal several important phenomena. Consistent with previous studies, the stress level in the plastic deformation stage decreases with increasing n at equivalent strain levels. For example, at a fixed strain of 0.05, the stress reaches approximately 150 MPa for n = 3, whereas it decreases to around 100 MPa for n = 10. However, the impact on hardening behavior becomes more pronounced in our low stress–strain regime. As the value of n increases, the rate of decrease in the stress–strain curve's slope diminishes progressively, indicating enhanced material hardening capability. A higher value of n corresponds to more slip system activity, which allows deformation to be distributed more uniformly within the material, thereby delaying the onset of strain localization. This behavior translates into improved mechanical properties, manifested through increased ductility and strength. Concurrently, the material's yield point becomes more distinctly defined. At n = 3, the yield point is less pronounced, with a gradual transition from elastic to plastic deformation. In contrast, at n = 10, the yield point is clearly defined at a strain of approximately 0.003, with a sharp increase in stress following yielding.

These phenomena suggest that under low stress and strain conditions, the selection of an appropriately reduced strain rate sensitivity coefficient is crucial for ensuring simulation accuracy. The observed strong dependence of hardening behavior on n values in this regime highlights the importance of parameter optimization for low-stress material simulations.

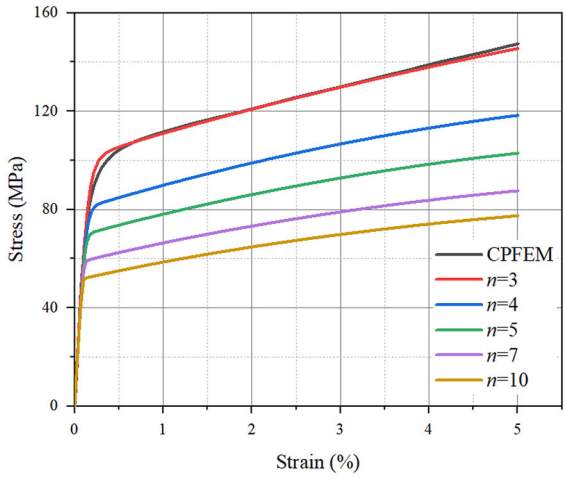

Fig. 12 Stress–strain curves for different values of n

4.6 The influence of tensile strain on GB fracture

As shown in Fig. 13, the applied strain significantly influences GB fracture behavior. In this study, strain was increased by adjusting the displacement rate from 0.075 to 0.15. Based on the contour maps of cumulative shear strain distribution, the tri-crystal model exhibited superior plasticity under low strain conditions. No crack formation was observed even at a local cumulative shear strain of 7.1%, whereas fracture initiated at a lower local cumulative shear strain of 3.85% under higher strain levels. Pole figure analysis reveals limited rotation of selected poles in low-strain conditions, with pole positions remaining stable. Under high strain, pole figure dispersion increases markedly, visually manifesting as pronounced pole spreading. However, the locations of GB fracture remain consistent across strain levels, with only minor variations in initial crack size. At 10% strain, the fracture propagation rate is notably slower than that observed at 8% strain.

This behavior originates from strain-dependent deformation mechanisms, i.e.: at low strain, the lattice undergoes reversible elastic deformation or limited plastic deformation with minimal crystallographic rotation. Only a few favorably oriented slip systems (those with higher Schmid factors) are activated, restricting localized grain rotations and stabilizing

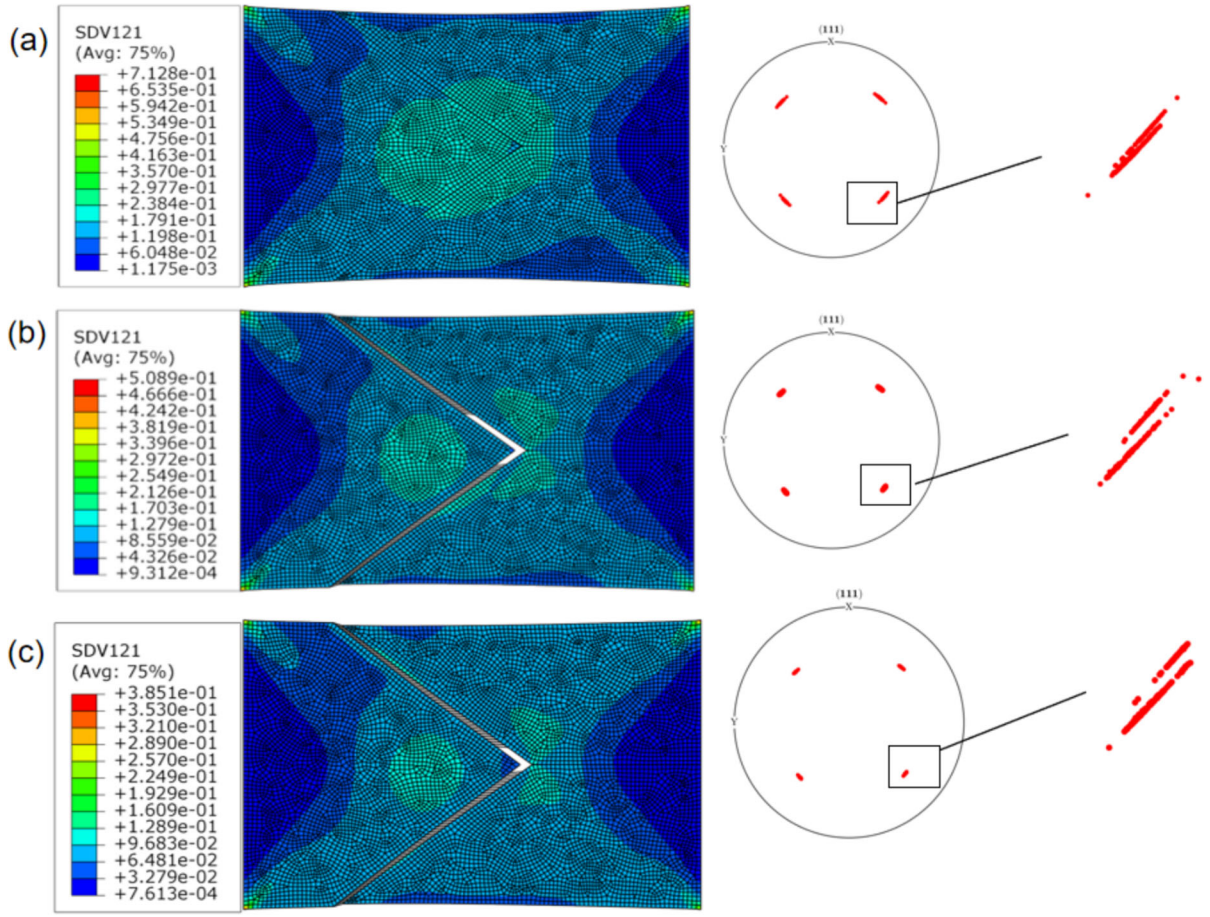

Fig. 13 Cumulative shear strain distribution and pole figures of different displacements: **a** 0.075 mm, **b** 0.12 mm and **c** 0.15 mm—SDV 121 represents the accumulative plastic strain

pole positions. At elevated strains, multiple slip systems activate, driving grain rotation until orientation stabilization occurs. The observed crack size discrepancy arises from increased stress intensity factors at crack tips under higher strain. According to the theory proposed by Rice, this promotes dislocation emission from crack tips, facilitating crack blunting and propagation. To maintain energy equilibrium, the initial crack size reduces correspondingly (Rice and Thomson 1974).

As shown in Fig. 14, the yield strength of the material increases with strain accumulation. Specifically, when the strain is increased from 5 to 8% and further to 10%, the yield strength rises by 18 MPa and 10 MPa, respectively, while the ductility decreases by 55% and 50%, respectively. This is attributed to the fact that under high strain rates, lattice dislocations

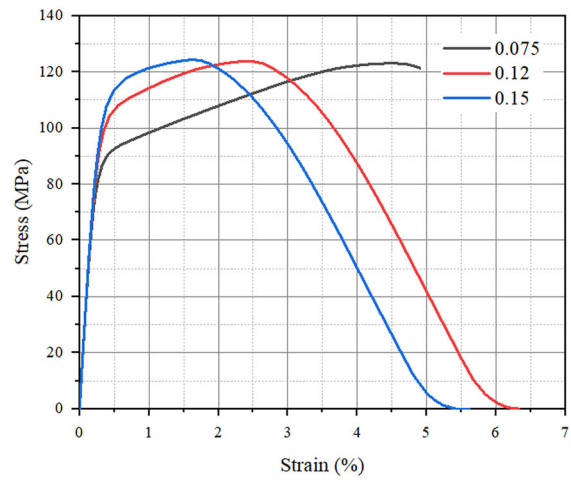

Fig. 14 Stress–strain curves for different rates of displacement

dissociate into GB dislocations, forming immobile configurations that intensify localized hardening and elevate yield strength. However, dislocation pileups near GBs generate stress concentrations, accelerating crack nucleation and thereby reducing ductility (Zhou et al. 2023). Conversely, lower strain rates provide sufficient time for dislocation cross-slip and GB sliding, enabling uniform stress redistribution and enhancing ductility (Goyal et al. 2020).

4.7 Effect of spatial arrangement in identical grain combinations

Due to the uniaxial tensile loading along the x-axis during simulation, stress concentration predominantly occurred at the interfaces between the primary grain (G1) and the adjacent grains (G2/G3). Therefore, three types of grains are selected and arranged in varying sequences to form distinct configurations for tensile simulations. Quantitative analysis (Fig. 15 and 16) reveals that the crystallographic orientation of G1 significantly impacts yield strength (3–20% variation) and exerts a more pronounced effect on fracture plasticity. While positional permutations of G2 and G3 grains show negligible influence ($< 1\%$ deviation) prior to reaching the ultimate tensile strength (UTS), a measurable difference ($\sim 2\%$) emerges near the UTS threshold. Subsequent observations of the stress contour plot for various combinations also reveal that altering the relative positions of the other two grains,

Table 3 Fracture energy under the stress–strain curves of various ternary crystalline configurations

Ternary crystalline configuration	Fracture energy (MJ/m^3)	Ternary crystalline configuration	Fracture energy (MJ/m^3)
S-Copper-Brass	2.59	Goss-Brass-P	7.09
S-Copper-Q	2.54	S-Copper-P	2.42
Brass-Goss-S	4.54	Brass-S-Goss	3.84
Copper-P-Q	2.62	Goss-S-Brass	5.97
Goss-Brass-Copper	5.63	S-Brass-Goss	4.02
Goss-Brass-S	6.38	S-Goss-Brass	3.91
Goss-Copper-S	5.31	Goss-Cube-Brass	7.02
P-S-Copper	2.39	Goss-S-Copper	5.05

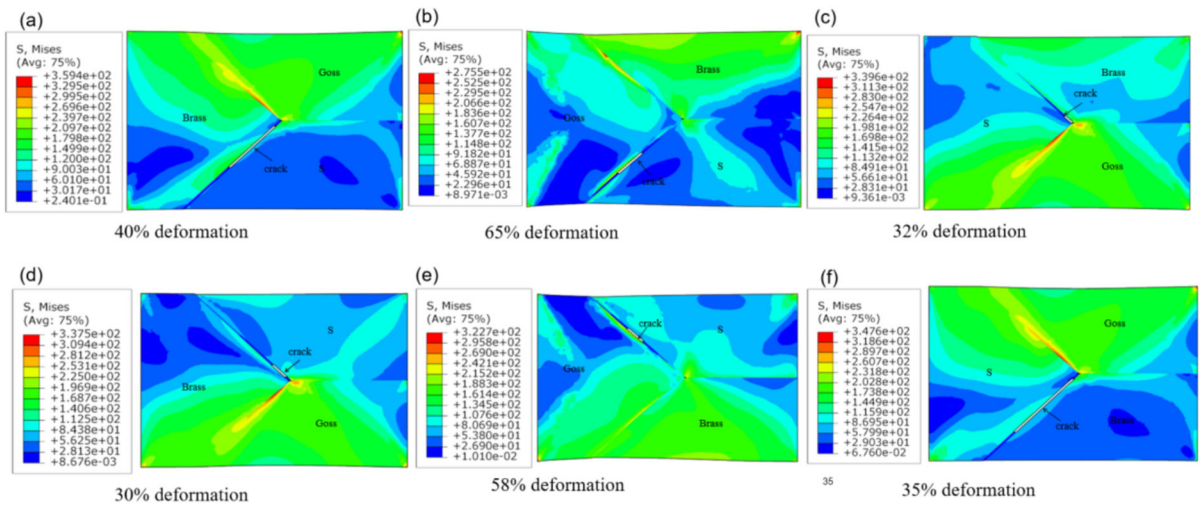

Fig. 15 Stress contour plots of different combinations and fracture strains: **a** Brass-Goss-S, **b** Goss-Brass-S, **c** S-Brass-Goss, **d** Brass-S-Goss, **e** Goss-S-Brass and **f** S-Goss-Brass

while maintaining the orientation of the first grain unchanged, exerts an 8–25% influence on the GB fracture velocity. The area under the stress–strain curve for each combination was subsequently calculated and recorded in Table 3. Area under the stress–strain curves of various ternary crystalline configurations. These observations underscore the necessity to account for both crystallographic orientation and topological configuration in multigrain modeling.

4.8 The influence of different grain orientations.

This study employs seven typical texture components to simulate the effects of different orientation combinations on grain boundaries, including: Brass (35°, 45°, 90°), Copper (90°, 35°, 45°), Goss (0°, 45°, 90°), Cube (0°, 0°, 0°), S (61°, 34°, 64°), Q (55°, 45°, 0°), and P (35°, 45°, 5°).

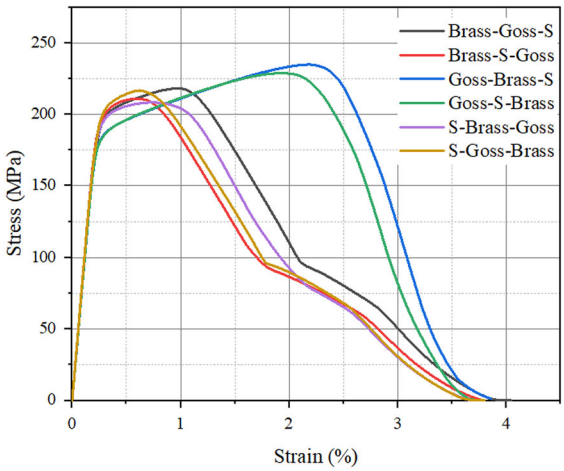

Fig. 16 Stress–strain curves at different positions in a tri-crystal system

From Fig. 17, it can be observed that the distinct crystallographic orientations of secondary grains significantly alter stress distribution patterns. Specifically, stress concentrations predominantly occur at both extremities of Copper-oriented grains, accelerating intergranular fracture initiation. In contrast, Brass-oriented grains exhibit more homogeneous stress distribution. Consequently, the Goss-Copper-Brass triple junction demonstrates intergranular fracture initiation at a maximum stress of 348.8 MPa, whereas the Goss-Cube-Brass configuration initiates fracture at a higher critical stress of 431 MPa, accompanied by altered fracture path localization. As shown in Fig. 17a, the pronounced stress concentration at the Goss-Brass interface directly corresponds to the initial fracture segment observed in the Goss-Cube-Brass assembly. This correlation provides critical insights for predicting intergranular fracture nucleation sites.

Comparative analysis of stress–strain responses in Fig. 18 reveals that the Goss-Copper-Brass combination exhibits higher stress levels than Goss-Cube-Brass below 0.016 strain, consistent with the Mises stress contour observations. This phenomenon arises from the dominant influence of secondary grain orientation modifications on stress redistribution mechanisms when maintaining constant primary and tertiary grain orientations. Specifically, the altered slip system activation and stress accommodation behavior in the secondary grain govern the macroscopic mechanical response.

Zhao et al. (2021) demonstrated that Goss and Cube orientations exhibit quasi-uniform stress fields aligned with the tensile axis, characterized by low orientation spread values. This homogeneous stress distribution stems from coordinated activation of multiple slip systems, enabling effective stress delocalization. Conversely, Copper and S orientations display marked

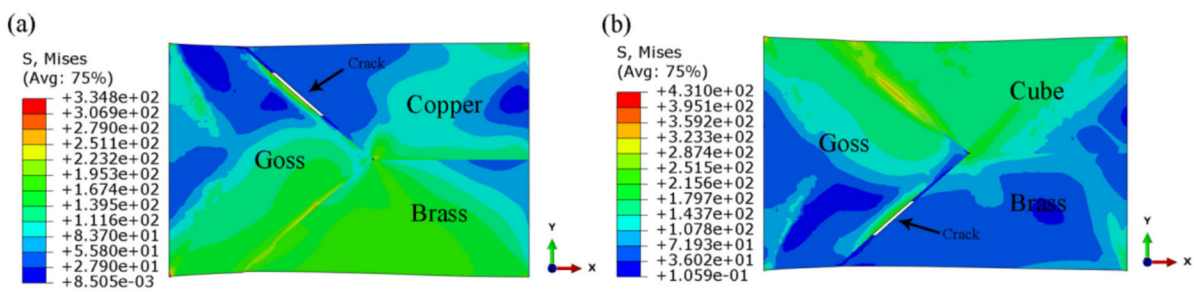

Fig. 17 **a** Goss-Copper-Brass GB fracture behavior and **b** Goss-Cube-Brass GB fracture behavior

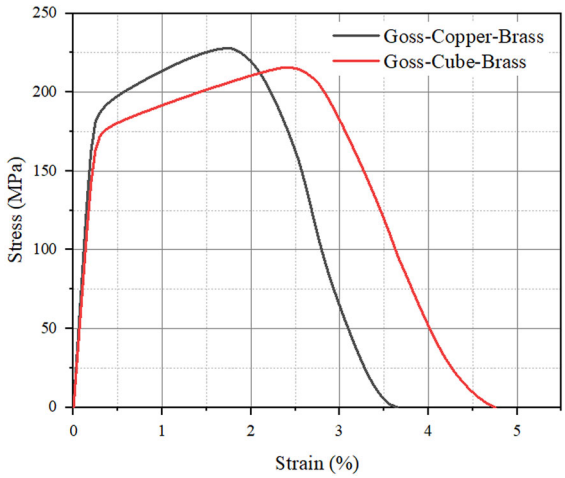

Fig. 18 Stress–strain curves of Goss-Copper-Brass and Goss-Cube-Brass tri-crystal combinations

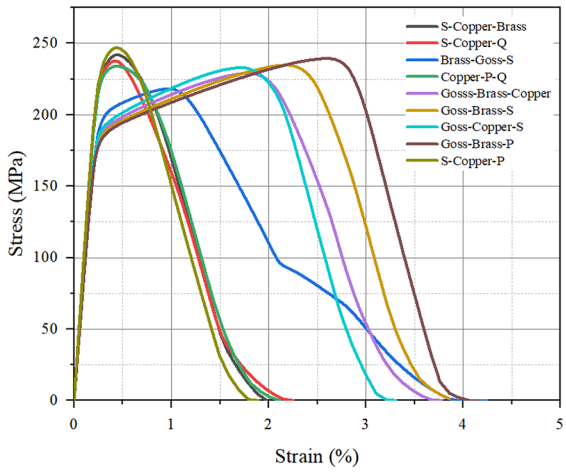

Fig. 19 Stress–strain behavior for different grain configurations

stress anisotropy with 45° inclined stress trajectories exhibiting origin symmetry, while Brass orientation manifests moderate asymmetry (approximately 30° deviation angle) observations corroborated by our simulations. Quantitative analysis reveals average stresses of 211.5 MPa and 204.3 MPa for Copper and Cube orientations respectively under equivalent strain conditions, elucidating the enhanced stress generation capacity of Goss-Copper-Brass configurations compared to Goss-Cube-Brass systems.

Subsequently, we can further examine the GB fracture sites. As mentioned above, due to the tensile loading along the *x*-axis, the GBs aligned with the *x*-axis (the contact surfaces between the second and third grains) have a relatively low likelihood of fracture. Therefore, the focus is on the contact surfaces between the first grain and the other two grains. According to the cloud map, fracture preferentially occurs at the Goss-Copper and Goss-Brass grain boundaries. This highlights that the location of GB fracture is determined by the orientations of the grains on either side of the boundary. Different orientations have varying effects on GB, yet cracks are more likely to initiate at boundaries between grains with a greater difference in orientation (Chen et al. 2013).

Finally, we assembled various triple-grain models with distinct crystallographic orientations and integrated their stress–strain curves in Fig. 19. As demonstrated in Fig. 19, configurations with S-textured or Copper-textured primary grains exhibit high yield strength but negligible ductility, with the S-Copper-P combination achieving the maximum yield strength. In contrast, other primary grain orientations sacrifice yield strength to enhance elongation, particularly the Goss-Brass-P configuration displaying optimal ductility. This observation aligns with Kumar et al. research documenting that high-angle grain boundaries substantially enhance strength at the probable expense of ductility (Kumar et al. 2003).

The reduced yield strength and improved elongation in Goss-oriented primary grain configurations further indicate that grain orientation misalignment alone cannot exclusively govern mechanical properties, as intragranular stress distribution constitutes a critical contributing factor. Conventionally, the integral area under stress–strain curves is recognized as a key indicator of comprehensive material performance. Quantitative analysis of these integrated areas in Table 3 reveals that the Goss-Brass-P configuration achieves the maximum value of 7.09, confirming its superior overall mechanical performance.

4.9 The prediction of the effect of GB thickness on GB fracture

For investigating the influence of GB thickness on material performance, a tensile strain of 8% was employed. As shown in Fig. 20, increasing the GB thickness from 0.5 to 1 resulted in a reduction of the maximum intergranular fracture stress from 256.6 MPa to 233.5 MPa, accompanied by diminished crack propagation. Further thickening to 2

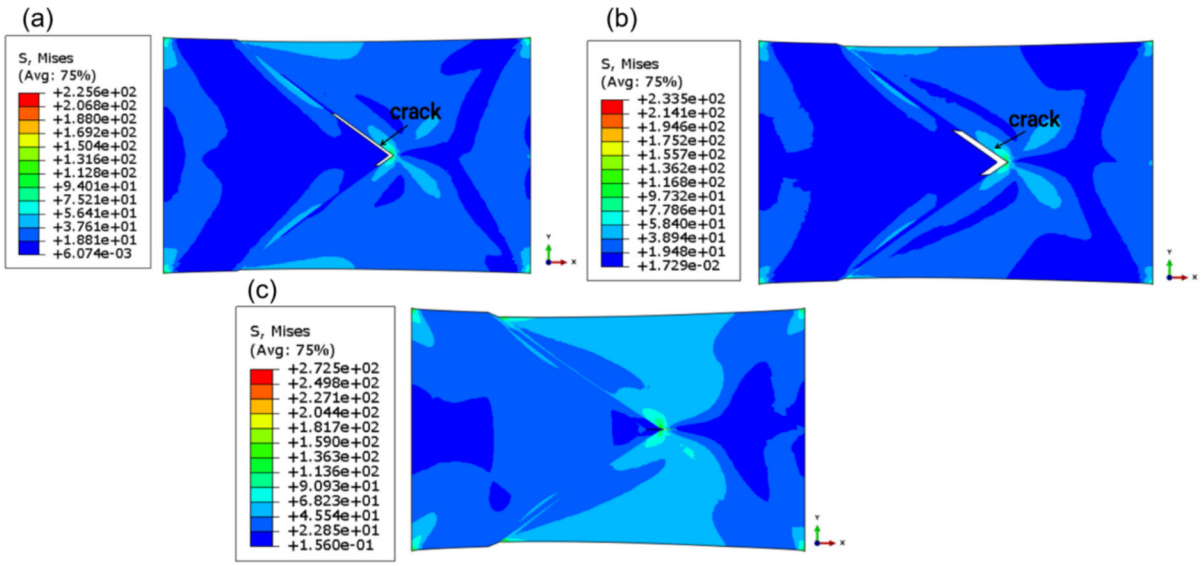

Fig. 20 Different GB thickness simulate: **a** cohesive = 0.5, **b** cohesive = 1, **c** cohesive = 2

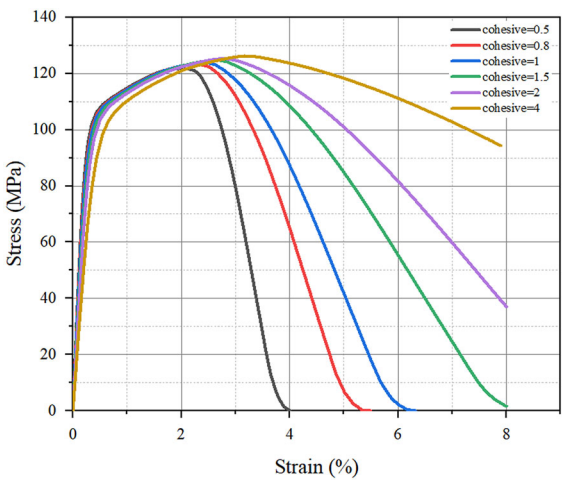

Fig. 21 Stress–strain curves with varying GB thicknesses

elevated the maximum stress to 272.5 MPa at 8% strain, with no significant boundary fracture observed except for a microcrack at the triple junction. Figure 21 demonstrates progressive enhancement of yield strength with increasing boundary thickness (from 0.5 to 2), as evidenced by the evolving stress distribution patterns. The ultimate tensile strength improved by 1.7% (from 120 to 122 MPa) and by 4.2% (from 120 to 125 MPa) under different conditions, respectively. Moreover, plasticity progressively improves. Their fracture energies are 3.54 MJ/m^3, 4.59 MJ/m^3, 5.22 MJ/m^3, 6.68 MJ/m^3, and 7.71 MJ/m^3, respectively. When cohesive is set to 4, the elastic modulus of the curve shows a significant decrease. Under equivalent strain in the elastic stage, strength reduction reaches up to 23.8%. These results indicate that when cohesive is less than 2, the comprehensive properties of triclinic crystals are positively correlated with GB thickness. Conversely, when cohesive exceeds 2, the properties are inversely proportional to GB thickness.

Notably, necking initiation and subsequent fracture progression commenced at strain levels of 0.02, 0.025, and 0.03 for the respective thickness configurations. This suggests that boundary thickening moderately enhances ductility, while halving boundary thickness accelerates crack propagation, reducing total failure duration by 30%. The diminished stress accommodation capacity of thinner boundaries, which restricts plastic deformation, explains the observed yield strength elevation, a phenomenon consistent with classical Hall–Petch relationships (Song et al. 2018; Zhu and Li 2010). This is because, within a certain range, dislocations dominate within grains. The thicker the GB that is, the greater the total area of active GBs the stronger its hindrance to dislocations, resulting in higher material strength and hardness. When dislocations enter GBs, thicker boundaries can coordinate mismatches between grains through their own deformation, thereby distributing stresses more uniformly. This enhances plasticity and reduces crack

initiation. However, when GB thickness exceeds a certain threshold, excessively thick boundaries become prone to shear slip, acting as crack initiation sites. When local stresses at these triple junctions surpass the fracture strength, premature microcracks form, leading to a reduction in material strength.

Intriguingly, fracture consistently localized at triple junctions regardless of boundary dimensions, further confirming that intergranular failure positioning depends solely on adjacent grain orientation pairs rather than boundary thickness (Kumar et al. 2003). This reinforces the dominant role of crystallographic mismatch over geometric factors in determining fracture path selection.

4.10 Simulation-based structural optimization design

From our triple crystal model, the relative positions of grains, grain orientation combination and GB thickness exist effect on strength and ductility of alloy. First, the relative positions of grains have very little effect on the properties of alloy. Figure 16 shows that the relative grain positions have little effect on tensile strength until it is reached, with only a 2% deviation observed after reaching tensile strength. So, the relative positions of grains can be ignored in material design. Second, orientation combination has a great effect on mechanical property of alloy. The Goss-Brass-P combination exhibits a maximal strain energy density of 7.09 MJ/m^3, followed by Goss-Cube-Brass also with an energy density of 7.02 MJ/m^3. Thus, the Goss-Brass-P orientation combinations represent a promising direction for alloy design. Some experimental studies also support the above grain orientation combination with well mechanical property. Experimental studies by Ma et al. (2014) demonstrate that the Goss-Brass-P orientation combination significantly enhances recrystallization quality and formability through synergistic effects, thereby establishing a foundation for homogenized mechanical properties. Furthermore, Hu et al. (2018) found that P-texture promotes uniform strain distribution and mitigates stress concentration. This provides a well support for the great product of strength and ductility of the Goss-Brass-P combination. In addition, GB thickness significantly affects material properties, which is also supported by the experimental study of Xu et al. (2023). This study shows that comprehensive property is positively correlated with GB thickness within a certain range. However, the correlation reverses beyond a threshold, yielding an appropriate GB thickness for optimal performance. Figure 21 demonstrates that the material exhibits optimal overall performance is achieved when the cohesive that determines GB thickness is set to 2. So, there exists a critical value for GB thickness that governs the mechanical properties of materials. Therefore, Goss-Brass-P orientation combinations together with GB thickness in the cohesive to 2 can form an outstanding overall mechanical properties.

5 Conclusions

In this study, we utilized a novel approach that integrates CPFE with cohesive elements to develop a tri-junction GB model. By incorporating cohesive elements into the GB interfaces, we simulated the damage and fracture behaviors, effectively modeling the intergranular fracture process. Furthermore, we examined the influence of various factors on GB fracture behavior. The key findings include:

- Parameter calibration via tensile modeling revealed the strain rate sensitivity exponent critically influences stress–strain response: increasing it from 3 to 10 enhances the yield point prominence and reduces yield strength from 100 to 52 MPa. The calibrated parameters enables tri-junction GB modeling with excellent convergence, effectively predicting intergranular fracture locations.
- Strain plays a crucial role in determining GB fracture and mechanical behavior, with increases from 5 to 8% and 10% boosting yield strength by 18 MPa and 10 MPa, respectively, but also reducing ductility by 55% and 50%. The data suggest that lower strain improve fracture resistance due to enhanced ductility, despite a modest decrease in strength.
- For the same grain configurations, variations in spatial arrangements predominantly impact mechanical performance. Significantly, the orientation of the primary grain can influence yield strength by 3–20%. Meanwhile, the positioning of secondary grains has a negligible effect on yield strength (less than 1%), yet it modulates tensile

strength by approximately 2% and fracture time by 8% to 25% through strain partitioning effects.

- Crystal orientation plays a significant role in determining GB fracture sites and material properties. We conducted an analysis focusing on two pivotal orientation combinations. The Goss-Copper-Brass combination exhibits higher stress levels compared to the Goss-Cube-Brass one. Additionally, different grain orientations result in distinct fracture sites within these combinations, such as a shift from the Goss-Copper boundary to the Goss-Brass boundary. After evaluating some possible combinations, we conclude that the Goss-Brass-P orientation combination yields the best mechanical properties, with a strain energy density reaching 7.09 MJ/m^3.
- GB thickness exhibits a positive correlation with the comprehensive properties within a certain range. However, yield strength decreases when the cohesive value exceeds 2. Through simulation calculations, we determined that setting the cohesive value to 2 yields the optimal overall material performance.

Acknowledgements Authors thank the financial support by the Hubei Provincial Major Science and Technology Special Project (2022AAA001), the Hubei Natural Science Foundation of China (2025AFD185), and the National Natural Science Foundation of China (51901073).

Authors contribution Xin Zhang: Writing-original draft, Methodology, Data curation, Conceptualization. Qi Zhao: Writing-review & editing, Supervision. Hongxia Zhang: Writing-review & editing, Supervision. ZhiPeng Zhai: Methodology, Xiang Chen: Methodology, Ying Hu: Methodology, Zhuo Han: Methodology, Nianfeng Zhang: Methodology, Yucheng Gui: Methodology, Magd Abdel Wahab: Writing-review & editing, Supervision.

Data availability The raw/processed data is available by contacting corresponding author on the reasonable request.

Declarations

Conflict of interest The authors declare that they have no known competing financial interests or personal relationships that could have appeared to influence the work reported in this paper.

References

Arsenlis A, Parks DM (1999) Crystallographic aspects of geometrically-necessary and statistically-stored dislocation density. Acta Mater 47(5):1597–1611

Arzt E (1998) Size effects in materials due to microstructural and dimensional constraints: a comparative review. Acta Mater 46(16):5611–5626

Asaro RJ, Needleman A (1985) Overview no. 42 texture development and strain hardening in rate dependent polycrystals. Acta Metall 33(6):923–953

Babicheva RI, Dmitriev SV, Bachurin DV et al (2017) Effect of grain boundary segregation of Co or Ti on cyclic deformation of aluminium bi-crystals. Int J Fatigue 102:270–281

Bessone JB, Salinas DR, Mayer CE et al (1992) An EIS study of aluminium barrier-type oxide films formed in different media. Electrochim Acta 37(12):2283–2290

Cantwell PR, Tang M, Dillon SJ et al (2014) Grain boundary complexions. Acta Mater 62:1–48

Chen YQ, Pan SP, Zhou MZ et al (2013) Effects of inclusions, grain boundaries and grain orientations on the fatigue crack initiation and propagation behavior of 2524–T3 Al alloy. Mater Sci Eng, A 580:150–158

Chou YT, Pande CS (1972) Effect of grain boundary dislocations on the slope of the Hall-Petch relation. Metall Mater Trans B 3:595–597

Du Y, Liu S, Zhang L et al (2011) An overview on phase equilibria and thermodynamic modeling in multicomponent Al alloys: focusing on the Al–Cu–Fe–Mg–Mn–Ni–Si–Zn system. Calphad 35(3):427–445

Figueiredo RB, Kawasaki M, Langdon TG (2023) Seventy years of Hall-Petch, ninety years of superplasticity and a generalized approach to the effect of grain size on flow stress. Prog Mater Sci 137:101131

Geng X, Gao J, Huang Y et al (2023) A novel dual-heterogeneous-structure ultralight steel with high strength and large ductility. Acta Mater 252:118925

Gorkaya T, Molodov KD, Molodov DA et al (2011) Concurrent grain boundary motion and grain rotation under an applied stress. Acta Mater 59(14):5674–5680

Goyal A, Doquet V, Pouya A (2020) Grain boundary sliding and strain rate sensitivity of coarse and fine/ultrafine grained 5083 aluminum alloys. Metall Mater Trans A Phys Metall Mater Sci 51:1109–1122

Hajshirmohammadi B, Khonsari MM (2020) Thermographic evaluation of metal crack propagation during cyclic loading. Theor Appl Fract Mech 105:102385

Hall EO (1951) The deformation and ageing of mild steel: III discussion of results. Proc Phys Soc Lond Sect B 64(9):747

Han Q, Yi X (2021) A unified mechanistic model for Hall-Petch and inverse Hall-Petch relations of nanocrystalline metals based on intragranular dislocation storage. J Mech Phys Solids 154:104530

Hill R, Rice JR (1972) Constitutive analysis of elastic-plastic crystals at arbitrary strain. J Mech Phys Solids 20(6):401–413

Hosford WF (2010) Mechanical behavior of materials. Cambridge University Press

Hu Y, Liu Z, Zhao Q et al (2018) P-texture effect on the fatigue crack propagation resistance in an Al-Cu-Mg alloy bearing a small amount of silver. Materials 11(12):2481

Huang W, Huo Q, Fang Z et al (2018) Damage analysis of hot-rolled AZ31 Mg alloy sheet during uniaxial tensile testing under different loading directions. Mater Sci Eng A 710:289–299

Hutchinson JW (1976) Bounds and self-consistent estimates for creep of polycrystalline materials. Proc R Soc Lond A Math Phys Sci 348(1652):101–127

Kocks UF, Mecking H (2003) Physics and phenomenology of strain hardening: the FCC case. Prog Mater Sci 48(3):171–273

Kramer L, Phillippi M, Tack WT et al (2012) Locally reversing sensitization in 5xxx aluminum plate. J Mater Eng Perform 21:1025–1029

Kumar KS, Van Swygenhoven H, Suresh S (2003) Mechanical behavior of nanocrystalline metals and alloys. Acta Mater 51(19):5743–5774

Künkler B, Düber O, Köster P et al (2008) Modelling of short crack propagation–transition from stage I to stage II. Eng Fract Mech 75(3–4):715–725

Liu J, Xiang C, Yuan H (2009) Prediction of 3D small fatigue crack propagation in shot-peened specimens. Comput Mater Sci 46:566–571

Ma M, Wang WX, Zhang JX et al (2014) The role of oriented growth in P texture development in Al-Mn-Mg aluminum alloy. J Mater Eng Perform 23(9):3257–3265

McHugh P, Asaro J, Shih C (1993) Texture development and strain hardening in rate dependent polycrystals. Acta Metall Mater 41:1461–1477

Miller WS, Zhuang L, Bottema J et al (2017) Recent development in aluminium alloys for the automotive industry. Mater Sci Eng A 280(1):37–49

Nasibullina OA, Tyusenkov AS, IOP Publishing (2019) Electronic and microscopic researches of dislocation structure of metal near crack top. IOP Conf Ser Mater Sci Eng 537(2):022023

Peirce D, Asaro RJ, Needleman A (1982) An analysis of nonuniform and localized deformation in ductile single crystals. Acta Metall 30(6):1087–1119

Peirce D, Asaro RJ, Needleman A (1983) Material rate dependence and localized deformation in crystalline solids. Acta Metall 31(12):1951–1976

Pouillier E, Gourgues AF, Tanguy D et al (2012) A study of intergranular fracture in an aluminium alloy due to hydrogen embrittlement. Int J Plast 34:139–153

Qu Y, Zhao Q, Ma D (2024) Texture evolution and stress formation behaviour during tensile deformation using crystal plasticity finite element method. Mater Sci Technol. https://doi.org/10.1177/02670836241246663

Randle V, Ralph B (1988) Grain boundary structure and mechanical properties. Rev Phys Appl 23(4):501–512

Rice JR, Thomson R (1974) Ductile versus brittle behaviour of crystals. Philos Mag A J Theor Exp Appl Phys 29(1):73–97

Rohith P, Sainath G, Srinivasan VS (2019) Effect of size temperature and strain rate on dislocation density and deformation mechanisms in Cu nanowires. Physica B 561:136–140

Rohoman MM, Zhou C (2025) Crystal plasticity modeling of dislocation density evolution in cellular dislocation structures. Metals 15:419. https://doi.org/10.3390/met15040419

Roters F, Eisenlohr P, Hantcherli L et al (2010) Overview of constitutive laws, kinematics, homogenization and multiscale methods in crystal plasticity finite-element modeling: theory, experiments, applications. Acta Mater 58(4):1152–1211

Song YF et al (2018) The effect of SiC addition on the dimensional stability of Al-Cu-Mg alloy. J Alloys Compd 750:111–116

Song Y, Zhang Q, Li H et al (2025) A novel cobweb-like subgrain structured Al-Cu-Mg alloy with high strength-plasticity synergy. Int J Plast 184:104178

Winning M, Gottstein G, Shvindlerman LS (2001) Stress induced grain boundary motion. Acta Mater 49(2):211–219

xiao M, Yao J, Huang C (2024) Fracture model of Al–Cu alloys with gradient crystals based on crystal plasticity. Metals 14(6):694

Xu Z, Li M, Zhang H et al (2023) Generalization of the hall-Petch and inverse hall-Petch behaviors by tuning amorphous regions in 2D solids. Natl Sci Open 2(3):20220058

Zhao N, Wang W, Liu Y (2018) Intergranular mechanical behavior in a blade groove-like component by crystal plasticity model with cohesive zone model. Eng Fract Mech 201:196–213

Zhao Q, Liu Z, Hu Y et al (2019) Texture effect on fatigue crack propagation in aluminium alloys: an overview. Mater Sci Technol 35(15):1789–1802

Zhao Q, Wahab MA, Ling Y et al (2021) Grain-orientation induced stress formation in AA2024 monocrystal and bicrystal using crystal plasticity finite element method. Mater des 206:109794

Zhao Q, Qu Y, Liu Z, Ke H, Jiang S, Wang X, Duan C, Zhai Z, Wahab MA (2024) Texture formation under control of S phase characteristic and tensile property of hot-rolling 2A12 aluminum alloy improved by Brass texture. Mater Sci Eng A 899:146445

Zhou S, Chen P, Zha M et al (2023) Sequential transmutation of prismatic dislocations during 112–2 twin-slip interaction in titanium. Scr Mater 236:115678

Zhu T, Li J (2010) Ultra-strength materials. Prog Mater Sci 55(7):710–757